

Electromagnetic Analog to Magic Angles in Twisted Bilayers of Two-Dimensional Media

Constantinos Valagiannopoulos^{*}

Department of Physics, School of Sciences and Humanities, Nazarbayev University, KZ-10000, Kazakhstan

(Received 7 June 2022; revised 9 August 2022; accepted 6 September 2022; published 5 October 2022)

Magic angles, namely, relative rotations between two parallel graphene flakes that create bigger periodic superlattices, are recently found to inherit the bilayer structure with exotic properties totally unknown to a single isolated graphite sheet. An electromagnetic analog to these regimes is provided by modeling the two monolayers of the same two-dimensional medium as anisotropic surface conductivities, which, if properly tilted, give substantial enhancement for the fields across the formed cavity. Such results may apply the paradigm of twistronics to nanophotonic design involving stacked optical materials, for serving a wide range of applications: from electromagnetic sensing and signal processing to radiative heat transfer and light harvesting.

DOI: 10.1103/PhysRevApplied.18.044011

I. INTRODUCTION

In certain materials and under strict conditions, electrons can move in an ordered and directional way without the need of voltage to push them; that is superconductivity, an exotic property of matter with huge applicability potential [1]. Such a fascinating effect is being studied for more than a century [2] and the developed theories usually thread it together with very low background temperatures [3]. Since the resistance into superconducting media drops to zero, the identification of the regime requires sophisticated experimental measurements [4] able to recognize the different phases into the host substance [5]. Finding a superconductor operating at higher temperatures has been the objective of long research efforts [6] involving substances like iron compounds [7] or boron-doped diamond [8] and others with similar crystalline lattices. In addition, alternative mechanisms of superconductivity being significantly different from conventional electron-phonon interactions, like the emergence of time-reversal-breaking states [9] or spin-orbit coupling between electron pairs [10], have been reported.

Unconventional superconductivity has been recently detected in a two-dimensional (2D) superlattice created by stacking two sheets of graphene that are twisted relatively to each other [11] at “magic” angles leading to flat electronic band structure [12]. This major discovery has been theoretically interpreted [13] and led to several follow-up findings concerning strong many-body correlations [14] and transitions between superconducting, insulating, or metallic phases [15]. The local density

of states and charge distribution in magic-angle twisted bilayer graphene has been also visualized [16] while the conditions for maximized electron interactions into the newly formed periodic superlattices have been identified [17]. Interestingly, explanations regarding that extraordinary magic-angle effect have been provided based on vanishing Fermi velocities [18], appearance of topological states [19] and phonon-mediated electron attraction [20].

In fact, magic angles in graphene bilayers ignited an alternative approach to manipulate the electronic properties of 2D media, labeled as “twistronics” [21] that has returned several premiums like quantized anomalous Hall effect [22], Dirac revival transitions [23] and Landau fans [24]. Correlated states in twisted flakes of 2D materials have been found tunable via external electric offsets [25], normal static magnetic bias [26] and in-plane alternating magnetic fields [27]. Furthermore, suitable relative rotations in bilayers have provided setups [28] serving a broad range of applications such as gate-controlled quantum interference via Josephson junctions [29] and manipulation of radiative heat transfer via exotic directional energy transport [30].

In this work, we consider two coupled, free-standing, uniaxially anisotropic monolayers of 2D materials being externally excited and placed at a short distance apart. By tilting properly their optical axes, the electromagnetic signal in between is maximized. Each flake is modeled as a photonic metasurface with specific complex surface conductivity tensor and it is found that, at these electromagnetically analogous magic-angle regimes, substantial enhancement of the field concentration at the bilayer is achieved. For realistic values of admittances emulated by common 2D media like graphene nanoribbons or black

* valagiannopoulos@gmail.com

phosphorus, the power into the cavity can be two decimal orders higher compared to the no-rotation scenario while such a score is decreasing with the distance between the monolayers. The reported results may shed light on the electromagnetic side of the effects occurring at the magic angles of bilayer superlattices and expand the context of twistrionics towards photonic applications such as signal control, light harvesting, or energy management at the nanoscale.

II. SURFACE CONDUCTIVITIES OF 2D MEDIA

A. Permissible value ranges

Anisotropy in 2D media is a prerequisite to having direction-dependent interactions with the incoming waves. If one homogenizes a single graphene monolayer, it can be well described by a sheet of surface impedance defined by the following Drude model [31]:

$$\sigma(\omega) = \eta_0 \frac{q^2 \mu_c}{\hbar^2 \pi} \frac{1}{1/\tau + i\omega}, \quad (1)$$

where a time dependence of the form $\exp(+i\omega t)$ is suppressed. The symbol η_0 is used for the wave impedance into free space while q is the electron charge. The notation μ_c is reserved for the chemical potential indicating the level of electron doping of graphene while τ is the relaxation time of particles. Formula (1) is mainly valid for THz waves and represents surface current controlled by electric field, in a directionally agnostic way. To create anisotropy one may utilize graphene nanoribbons of different features, as depicted in Fig. 1(a); thus, there are two different surface admittances $\sigma_A \neq \sigma_B$ to play with. As a result, the effective conductivities along the two major axes (X, Y) are written as [32]

$$\sigma_X = r\sigma_A + (1-r)\sigma_B, \quad (2a)$$

$$\sigma_Y = \frac{\sigma_A\sigma_B}{(1-r)\sigma_A + r\sigma_B}, \quad (2b)$$

where $0 < r < 1$ is the relative portion of the first nanoribbon across the periodic configuration.

It should be stressed that the losses of the 2D materials are described via the real part of the surface admittance σ , which is positive for lossy structures. On the other hand, $\text{Im}[\sigma] > 0$ describes a dielectric response while $\text{Im}[\sigma] < 0$ indicates plasmonic behavior. To understand what values of $\text{Im}[\sigma]$ are attained by a graphene sheet at the THz regime, in Fig. 2(a), we represent it as a function of the operational frequency ω and the chemical potential μ_c , in terms of $1/\eta_0$. One clearly notices that, across the considered band, graphene exhibits plasmonic response that gets stronger for increasing μ_c . In particular, the 2D medium is turned into more metallic at the range $1 \text{ THz} < \omega/(2\pi) < 10 \text{ THz}$ and these values of $\text{Im}[\sigma]$ can become smaller

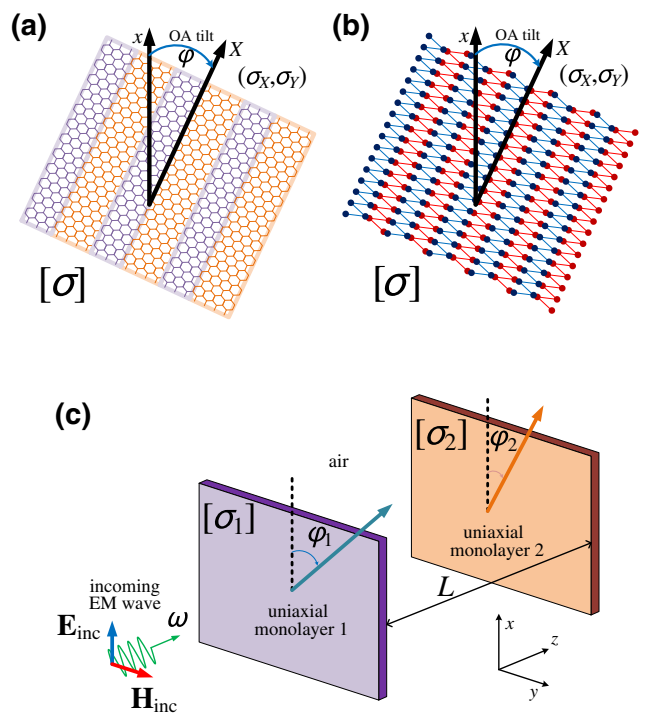


FIG. 1. Illustrative representation of anisotropic graphene monolayer, with optical axis (OA) tilted by angle φ , comprised of graphene nanoribbons with different doping levels. The two surface conductivities along the major axes (X, Y) are denoted by (σ_X, σ_Y) and form an effective conductivity tensor $[\sigma]$ expressed in the global coordinate system (x, y) . (b) Same as Fig. 1(a) for a black phosphorus monolayer. (c) Schema of two coupled monolayers of the same uniaxially anisotropic 2D medium, characterized by effective surface conductivity tensors $[\sigma_1], [\sigma_2]$ and optical tilts (φ_1, φ_2) , being kept at distance L apart and excited normally by an electromagnetic (EM) wave of angular frequency ω .

(more negative) for larger doping amounts. Similarly, in Fig. 2(b), we show $\text{Im}[\sigma]\eta_0$ across the regarded THz spectrum of ω but with respect to particles' relaxation time τ ; the distribution pushes enhanced plasmonic behavior towards higher frequencies compared to Fig. 2(a). It is, thus, clear that for a realistic set of parameters (μ_c, τ) , the conductance of graphene can be regulated to cover an extended value range. It is also worthwhile to note, with slight modifications, σ is given by more sophisticated models [33] leading to substantially positive $\text{Im}[\sigma]\eta_0$ and, accordingly, suggesting significant dielectric effects. Consequently, it is demonstrated that in the case of graphene, the variation domain of $\text{Im}[\sigma]$ includes magnitudes of several multiples of $1/\eta_0$ both of negative and positive signs.

Anisotropy can be also built in like in the case of black phosphorus, which is characterized by a zigzag structure of phosphorene along one dimension while the molecules are arranged at an armchair pattern along the other one. A top

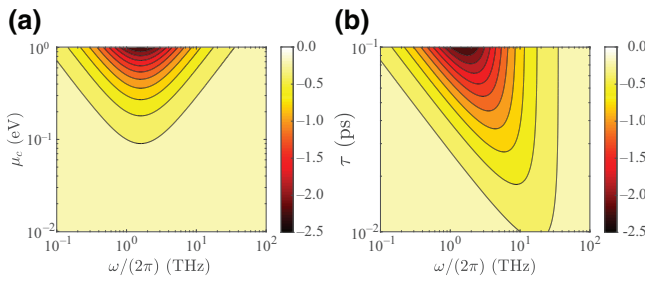


FIG. 2. Variation of the imaginary part of the normalized conductivity at a graphene monolayer $\text{Im}[\sigma]\eta_0$ in the contour plot with respect to the operational frequency $\omega/(2\pi)$ in THz and (a) chemical potential μ_c in eV ($\tau = 0.1$ ps), (b) relaxation time τ in ps ($\mu_c = 1$ eV).

view of such a 2D material is depicted in Fig. 1(b), where the red-colored atoms are located below the blue-colored ones and, in this sense, a uniaxial preference is achieved. In Fig. 3, we consider a stack of several monolayers making phosphorene of (small) thickness d , and extract the surface admittances across the two indicated axes (X, Y) based on *ab initio* calculations [34]. In Fig. 3(a) we represent $\text{Im}[\sigma_X]$, namely the conductivity along the zigzag direction, with respect to the oscillation frequency $50 \text{ THz} < \omega/(2\pi) < 200 \text{ THz}$ and the size d of the sample. It is clear that the dielectric response gets stronger for thicker layers across the entire considered band and also $\text{Im}[\sigma_X]$ increases with the operational frequency. In Fig. 3(b) we show $\text{Im}[\sigma_Y]$ (armchair direction) at the same parametric map and notice that the quantity remains positive and possesses larger values compared to Fig. 3(a). Despite the fact that the variation trends are similar, we understand that substantial anisotropy $\text{Im}[\sigma_X] \neq \text{Im}[\sigma_Y]$ can be routinely achieved and each of the admittances may take values as high as many multiples of $1/\eta_0$.

Once the optical axis gets tilted by angle φ , as indicated in Figs. 1(a) and 1(b), the surface conductivity tensor of the

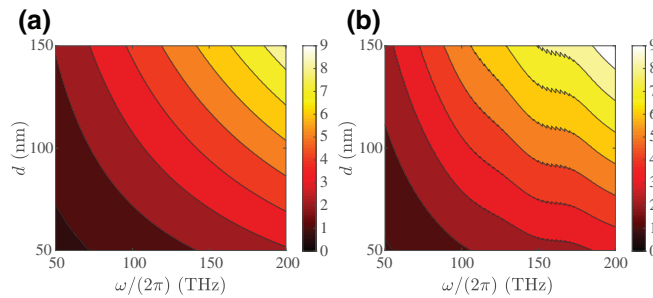


FIG. 3. Variation of the imaginary part of the normalized conductivities of a black phosphorus stacked monolayer in a contour plot with respect to the operational frequency $\omega/(2\pi)$ in THz and the thickness d of the stack in nm, along (a) X axis ($\text{Im}[\sigma_X]\eta_0$) and (b) Y axis ($\text{Im}[\sigma_Y]\eta_0$). The represented values are based on *ab initio* data [34].

monolayer $[\sigma]$ expressed in the global coordinate system (x, y) is trivially found as

$$[\sigma] = \begin{bmatrix} \bar{\sigma} + \Delta\sigma \cos(2\varphi) & \Delta\sigma \sin(2\varphi) \\ \Delta\sigma \sin(2\varphi) & \bar{\sigma} - \Delta\sigma \cos(2\varphi) \end{bmatrix}, \quad (3)$$

where $\bar{\sigma} = (\sigma_X + \sigma_Y)/2$ and $\Delta\sigma = (\sigma_X - \sigma_Y)/2$. The notation $[\sigma] \equiv \begin{bmatrix} \sigma_{xx} & \sigma_{xy} \\ \sigma_{yx} & \sigma_{yy} \end{bmatrix}$, regarding the respective elements of the 2×2 matrix, can be used interchangeably.

Uniaxial electromagnetic metasurfaces can be categorized based on the conductivities along their major axes (σ_X, σ_Y). With reference to Eq. (2), and under the assumption of lossless constituent media ($\text{Re}[\sigma_A] = \text{Re}[\sigma_B] = 0$), one may formulate the map of Fig. 4(a) where the signs of $\text{Im}[\sigma_X], \text{Im}[\sigma_Y]$ are presented in each domain across the plane of imaginary parts of (σ_A, σ_B) representing the two strips shown in Fig. 1(a). If the signs of the imaginary parts of (σ_X, σ_Y) are opposite, the monolayer is characterized by hyperbolic dispersion relation [35]; in contrast, if $\text{Im}[\sigma_X]\text{Im}[\sigma_Y] > 0$, the metasurface is called elliptic.

By inspection of Fig. 4(a), where the two materials participate with equal portions ($r = 0.5$), one clearly infers that hyperbolic regime (orange and light blue color) is feasible only when $\text{Im}[\sigma_A]\text{Im}[\sigma_B] < 0$. Moreover, a comparison between the magnitudes $|\text{Im}[\sigma_A]|, |\text{Im}[\sigma_B]|$ determines along which direction (X, Y) the response is dielectric, and across which plasmonic. In Fig. 4(b), we reduce the filling factor of the first 2D medium (A) in favor of the second one (B) by selecting $r = 0.25$ and we realize that the domains giving hyperbolic effective properties get shrunk and in most cases the metasurface is elliptic (deep blue and brown colors); such a feature is anticipated since the structure becomes less anisotropic. In this sense, it is natural that the most interesting results appear for hyperbolic regimes since the whole “magic-angle” switch is due to the effective in-plane anisotropy of the metasurface. Obviously, these hyperbolic parametric regions vanish for $r \rightarrow 0, 1$ while a symmetry with respect to the origin $\text{Im}[\sigma_A] =$

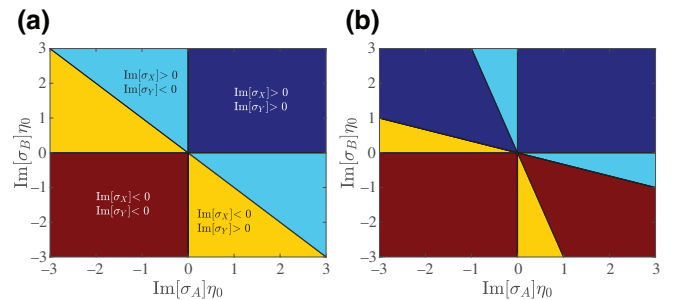


FIG. 4. Domains across the map of the imaginary parts of each strip's conductivities ($\text{Im}[\sigma_A]\eta_0, \text{Im}[\sigma_B]\eta_0$) corresponding to different signs of the imaginary parts of effective admittances (σ_X, σ_Y). Different filling factors of the first 2D medium into the second one are considered: (a) $r = 0.5$, (b) $r = 0.25$.

$\text{Im}[\sigma_B] = 0$ is observed, remarking the reciprocity in the location of the two strips.

Usually hyperbolic media possess a richer repertoire of responses when interacting with electromagnetic waves [36]; indeed, for the simplest scenario of normal incidence on a planar infinitesimally thin interface, a hyperbolic structure affects each of the in-plane field components in a dissimilar way imposing a 180° phase shift due to the different sign of the conductivities. Therefore, both the reflective and transmissive waves can acquire polarizations and phases that, in a conventional (elliptic) scenario, call for anisotropic bulk materials of nonzero thicknesses [37].

B. Structure feasibility

The feasibility of the structure depicted in Fig. 1(a) is a matter that should be discussed since we regard two strips of 2D media posed side-by-side with different characteristics and at subwavelength distances. The fabrication of such setups, however challenging, can be well approximated by graphene nanoribbons with small airgaps in between that will be taken into account (with zero local admittance, $\sigma = 0$) in the effective anisotropy of the device. As far as the nanoribbons themselves are concerned, they can be constructed in a variety of ways such as application of voltage bias along the zigzag direction of the graphene crystalline grid [38], unzipping of periodically placed carbon nanotubes [39] or selective growth of carbide surfaces with the help from homochiral polymers as precursors [40]. Thin graphene nanotapes are fabricable at different planes in cage layouts each side of which can be doped at unequal levels [41] while adjacent carbon segments of different homogenized chemical properties can be chemically solution synthesized [42].

Apart from graphene, nanoribbons of other 2D media are also constructible. In particular, subwavelength strips of black phosphorus of Fig. 1(b), which is already anisotropic as demonstrated by Fig. 3, can be produced via ionic scissoring of macroscopic crystals [43]. Interestingly, electrochemical unzipping of single-crystal black phosphorus into zigzag-phosphorene nanobelts, as well as growth of elongated nanosheets via an oxygen-driven mechanism, have been reported [44]. Finally, even hexagonal boron-nitride nanosegments, mostly terminated with zigzag edges, can be produced via unwrapping multi-walled nanocylinders of controllable vacancy defects and conducting edge states [45].

It should be noted that Figs. 2 and 3 are included mostly for demonstration purposes to define the permissible ranges of surface conductivities employed in the subsequent numerical results; we do not necessarily plan on using these specific 2D materials. However, we advocate that combinations of surface conductivities (σ_X, σ_Y) of different signs along each dimension can be achieved and, thus, we may sweep the two parameters as if they

were independent of each other. Indeed, we just refer to multiple methods for constructing nanoribbons of several 2D media, regardless of their dielectric or metallic behavior they exhibit and place them one next to the other, even with some inevitable (but small) physical separation.

Additionally, alternating plasmonic and dielectric response across a continuous plane of graphene or another 2D material can be emulated in a variety of ways. More specifically, different substrates have been utilized above a flake to constitute a coupler between consecutive layers of alternating nature [46] while similar interactions are observed in graphene nanoribbons sitting on suitable bases, accompanied by radiative damping [47]. Furthermore, sinusoidal patterning of the boundaries of nanobelts yields periodic strips of graphene interacting with the substrate in a thickness-dependent fashion that may enable each segment to respond differently with the background electric field [48]. Finally, the design of multimode interference splitters comprising dielectric strips on a plasmonic graphene monolayer has been proposed in an on-chip implementation [49].

III. COUPLED MONOLAYERS

A. Boundary value problem

Let us consider the structure depicted in Fig. 1(c) where two coupled flakes of the same 2D medium with different twist angles (φ_1, φ_2) are located at distance L between them. The effective surface admittance tensors of each monolayer are denoted by $[\sigma_1], [\sigma_2]$ in the coordinate system (x, y, z) defined in Fig. 1(c), according to Eq. (3). If the dimer is normally illuminated by an electromagnetic wave, traveling along the z axis, the electric field into the cavity takes the form

$$\mathbf{E} = (\hat{\mathbf{x}}A_x + \hat{\mathbf{y}}A_y)e^{-ik_0z} + (\hat{\mathbf{x}}B_x + \hat{\mathbf{y}}B_y)e^{+ik_0z}, \quad (4)$$

where $k_0 = \omega/c = 2\pi/\lambda$ is the wave number and c is the speed of light into vacuum. The weights $\{A_x, A_y, B_x, B_y\}$ are determined in the following. The x -polarized incident electric field is taken of unitary amplitude: $\mathbf{E}_{\text{inc}} = \hat{\mathbf{x}}e^{-ik_0z}$ while the reflected and transmitted components are written as $\mathbf{E}_{\text{ref}} = (\hat{\mathbf{x}}R_x + \hat{\mathbf{y}}R_y)e^{+ik_0z}$ and $\mathbf{E}_{\text{tran}} = (\hat{\mathbf{x}}T_x + \hat{\mathbf{y}}T_y)e^{-ik_0z}$, respectively, where $\{R_x, T_x, R_y, T_y\}$ are the complex reflection and transmission coefficients along each of the in-plane directions. Obviously, the magnetic field \mathbf{H} is found via imposing Faraday's law: $\mathbf{H} = \frac{i}{k_0\eta_0}\nabla \times \mathbf{E}$, into each of the regarded three vacuum regions.

After enforcing the boundary condition for continuity of the electric field at $z = 0$: $\hat{\mathbf{z}} \times (\mathbf{E} - \mathbf{E}_{\text{inc}} - \mathbf{E}_{\text{ref}}) = \mathbf{0}$, one obtains

$$R_x = A_x + B_x - 1, \quad R_y = A_y + B_y. \quad (5)$$

Similarly, the boundary condition for continuity of the electric field at $z = L$: $\hat{\mathbf{z}} \times (\mathbf{E}_{\text{tran}} - \mathbf{E}) = \mathbf{0}$ yields two

scalar formulas (one for each direction) expressing the respective transmission coefficients in terms of the field coefficients into the cavity, Eq. (4); in particular,

$$T_x = A_x + B_x e^{+2ik_0 L}, \quad T_y = A_y + B_y e^{+2ik_0 L}. \quad (6)$$

The inhomogeneous boundary conditions referring to the discontinuity of the magnetic fields by the local electric fields multiplied with the conductivity tensors, are mathematically expressed as [50]

$$\hat{\mathbf{z}} \times (\mathbf{H} - \mathbf{H}_{\text{inc}} - \mathbf{H}_{\text{ref}})|_{z=0} = [\sigma_1] \cdot \mathbf{E}|_{z=0}, \quad (7a)$$

$$\hat{\mathbf{z}} \times (\mathbf{H}_{\text{tran}} - \mathbf{H})|_{z=L} = [\sigma_2] \cdot \mathbf{E}|_{z=L}, \quad (7b)$$

where the z component is ignored in the incorporated vectors. Note that Eqs. (7a), (7b) correspond to

Kirchoff's law for the flowing current in the presence of voltage-controlled current source. By imposing them, four scalar equations are deduced, since each of Eq. (7) is of vectorial nature. The formulated 4×4 linear system with respect to the complex coefficients $\{A_x, A_y, B_x, B_y\}$, which are functions of angles (φ_1, φ_2) , is given by Eq. (8) below. The respective elements of the 2×2 matrices $[\sigma_1]$ and $[\sigma_2]$ appear in the expression.

In this way, the field between the two monolayers is derived in a rigorous way and constitutes the unique solution to the defined boundary value problem. Accordingly, no approximation is made and evanescent modes are not excited into the cavity since the structure is illuminated by a normally incident plane wave (wave number k_0 into free space).

$$\begin{bmatrix} \frac{2}{\eta_0} + \sigma_{1xx} & \sigma_{1xy} & \sigma_{1xx} \\ \sigma_{1xy} & \frac{2}{\eta_0} + \sigma_{1yy} & \sigma_{1xy} \\ e^{-ik_0 L} \sigma_{2xx} & e^{-ik_0 L} \sigma_{2xy} & e^{+ik_0 L} \left(\frac{2}{\eta_0} + \sigma_{2xx} \right) \\ e^{-ik_0 L} \sigma_{2xy} & e^{-ik_0 L} \sigma_{2yy} & e^{+ik_0 L} \sigma_{2xy} \end{bmatrix} \cdot \begin{bmatrix} A_x \\ A_y \\ B_x \\ B_y \end{bmatrix} = \frac{2}{\eta_0} \begin{bmatrix} 1 \\ 0 \\ 0 \\ 0 \end{bmatrix}. \quad (8)$$

B. Field concentration metric

The spatial average of light intensity across the form cavity can be an indicator of how powerful the signal in between the two coupled flakes as follows

$$\begin{aligned} P(\varphi_1, \varphi_2) &\equiv \frac{1}{L} \int_0^L |\mathbf{E}(z)|^2 dz \\ &= |A_x|^2 + |A_y|^2 + |B_x|^2 + |B_y|^2 \\ &\quad + 2 \frac{\sin(k_0 L)}{k_0 L} \operatorname{Re} \left[(A_x B_x^* + A_y B_y^*) e^{-ik_0 L} \right]. \end{aligned} \quad (9)$$

Therefore, a meaningful metric for detecting the electromagnetic analog of “magic angles” would be the ratio $Q = P(\varphi_1, \varphi_2)/P(\varphi_1, \varphi_1)$, which expresses the enhancement in the concentrated power under the relative in-plane rotation by an angle $(\varphi_2 - \varphi_1)$ and will be maximized in the adopted optimization scheme. To avoid multiple identical optimal setups, we sweep the first angle over the entire circle, $-90^\circ < \varphi_1 < 90^\circ$, and the second over half the range, $0^\circ < \varphi_2 < 90^\circ$.

One may wonder how the field concentration defined via Eq. (9) compares with power accumulation reported through approaches involving the developed acoustic modes at very subwavelength distances L . Indeed, graphene bilayers constitute mechanical nanoresonators

that are proposed to operate at the resonance frequency of breathing modes [51] while Moiré interlayer potential boosts the intensity of asymmetric modes for similar setups [52]. Interestingly, substantial increase of the phonon density of states has been observed by regulating the lattice twists at various stacking configurations [53]. However, the recorded scores in the aforementioned works, are not comparable with our computed quantities P in Eq. (9), for two major reasons. (i) We are considering macroscopic electromagnetic fields and evaluate the energy of the signal accumulated between the monolayers while most of the other techniques study in-plane acoustic phonons and determine the local potential energy of the particles. (ii) We excite unilaterally the structure via a normally incident beam while other the approaches consider a source-free version of the setup and investigate the modes of phonon dispersion.

Another issue is the suitability of the selected metric Q and how the signal concentration $|\mathbf{E}|^2$ may be related with the appearance of superconductivity or alternative phase-changing effects. In fact, several experimental studies have shown that increased local fields create a fertile ground for the particles to behave in various exotic ways and modify abruptly their current states. In particular, electric-field-induced superconductivity in an insulator by using electric-double-layer gating at organic electrolytes

has been reported [54] while the application of strong fields effectively contribute to the high-temperature superconductivity in ultrathin iron selenides [55]. High magnetic fields have also been found responsible for enhancing electron-electron interaction in systems with low carrier density [56] and may stabilize superconductivity because transition temperature increases with the applied intensity [57]. Of course, in most of the aforementioned works, the electric or magnetic fields are static biases contrary to the considered electromagnetic waves of our approach that oscillate with frequency ω . However, matter waves, representing high-energy particles, oscillate much faster and may perceive the background fields as time invariant.

In any case, it should be remarked that maximization of the power P across the considered cavity or optimization of the adopted metric Q is not necessarily accompanied by a transition in the behavior of the traveling electrons. Our analysis follows the classical electrodynamics principles studying electromagnetic fields coupled with homogenized media and not isolated particles trading with crystalline structures. Therefore, in the framework of the regarded model, we do not demonstrate superconductivity or other modification in the way the electrons interact with matter. We simply advocate that a significant value in Q enables the respective pair of optical axes tilts (φ_2, φ_1) to be characterized “magic angles” in the electromagnetic sense. Indeed, these rotations create a dramatic switch in the operation of the cavity since a huge change in a fundamental quantity like the accumulated power is observed.

IV. MAGIC ANGLES

A. Optimal designs

In Fig. 5(a), we show the variation of Q across the map of two angles (φ_1, φ_2) for 2D flakes of plasmonic conductivity along X axis ($\sigma_X = -i/\eta_0$) and dielectric response along Y axis ($\sigma_Y = 4i/\eta_0$). The metric Q indicates that the signal can be enhanced several times simply by

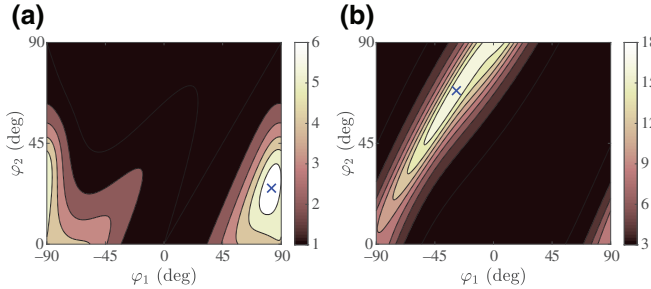


FIG. 5. Process of detecting the magic angle that maximizes the signal enhancement Q . The metric Q is shown across the map of the optical axes twists (φ_1, φ_2) and the magic angle is denoted by a blue \times pointer for different axial surface conductivities: (a) $\sigma_X = -i/\eta_0$, $\sigma_Y = 4i/\eta_0$ and (b) $\sigma_X = 4i/\eta_0$, $\sigma_Y = -4i/\eta_0$. Distance between monolayers: $L = 0.01\lambda$.

rotating the two monolayers and the pair of magic angles (φ_1, φ_2) giving maximal power concentration is indicated by a blue marker \times . In Fig. 5(b), we assume dielectric behavior along X axis and metallic along Y axis and more substantial values for the field enhancement metric Q , being proportional to the structure’s interaction with the incident x -polarized wave, are recorded. This time the optimal regime is achieved when the two flakes are rotated around opposite directions ($\varphi_1\varphi_2 < 0$) and a very elongated oblique parametric “plateau” is formed around the blue marker. Therefore, larger sensitivity of the bilayer signal accumulation capability, with respect to the optical tilts, is expected.

If we repeat the computations behind Figs. 5(a) or 5(b) for numerous pairs of major surface conductivities (σ_X, σ_Y) , we can store the maximal scores Q in order to represent them in graphs where the optimization with respect to angles (φ_1, φ_2) is implied. In Fig. 6, we consider two lossless monolayers ($\text{Re}[\sigma_X] = \text{Re}[\sigma_Y] = 0$) and show the greatest possible field enhancement as a function of the imaginary parts of the two surface conductivities ($\text{Im}[\sigma_X], \text{Im}[\sigma_Y]$). In other words, each point on the regarded map is the result of an optimization on the major parametric plane of tilts (φ_1, φ_2) . The depicted quantity possesses much higher magnitudes compared to Fig. 5, which is natural since an extensive assortment of surface conductivity combinations has been investigated.

In Fig. 6(a), we consider an interlayer distance $L = 0.05\lambda$ and the maximum signal concentration is recorded when the used monolayers are hyperbolic ($\text{Im}[\sigma_X]\text{Im}[\sigma_Y] < 0$) and, especially, when one of the two imaginary parts approaches the value $\text{Im}[\sigma_X] \cong 3.5/\eta_0$ while the other satisfies the inequality $\text{Im}[\sigma_Y] < -1.5/\eta_0$. In Fig. 6(b), the two monolayers are located much closer to each other ($L = 0.01\lambda$) and the average field into the cavity gets amplified while the optimal contrast between the two major admittances (σ_X, σ_Y) increases further to push the global optimum outside of the regarded map.

The reasoning behind the high scores achieved by hyperbolic coupled flakes concern two factors: (i) the optically

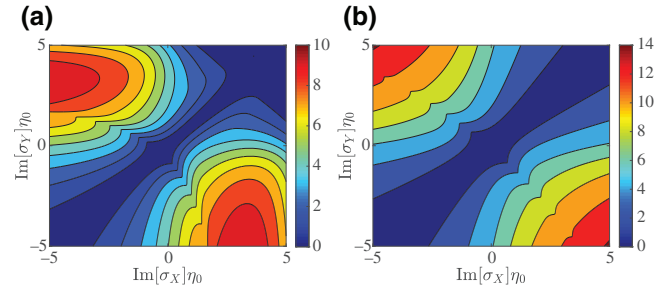


FIG. 6. Maximum signal enhancement $10 \log_{10} Q$ (in decibels) by regulating the optical twists (φ_1, φ_2) as a function of the imaginary parts of normalized surface conductivities $(\text{Im}[\sigma_X]\eta_0, \text{Im}[\sigma_Y]\eta_0)$, for two different distances between the two lossless monolayers: (a) $L = 0.05\lambda$ and (b) $L = 0.01\lambda$.

small distance between the two monolayers ($L \ll \lambda$) and (ii) the phase difference imposed to the produced waves due to the opposite signs of admittances ($\text{Im}[\sigma_X]\text{Im}[\sigma_Y] < 0$). Indeed, the tiny thickness of the cavity means that there is no phase shift between the two reflections (firstly of the incident wave by the first metasurface and secondly of its transmitted wave by the second metasurface). As a result, a matched regime (null aggregate reflection), which is usually an indication of strong field into the bilayer, may occur only if the dispersion is hyperbolic otherwise the two reflections never cancel each other. When it comes to the assumption that matching can be treated as a precondition for large accumulated power P , it is explained by the empty area between the flakes, which does not permit the development of large local fields as in the case of a dense dielectric filling [58].

In Fig. 7, we assume that the monolayer is lossy along the Y axis without reactive part ($\text{Im}[\sigma_Y] = 0$) and lossless along the X axis. In Fig. 7(a), the size of the bilayer is kept fixed at $L = 0.05\lambda$ and the highest metric Q after sweeping all possible in-plane rotation angles (φ_1, φ_2) is represented on $(\text{Im}[\sigma_X], \text{Re}[\sigma_Y])$ plane. However, the performance is substantially suppressed compared to the respective Fig. 6(a) due to the apparent Ohmic effects. The best scores are found either for an overall lossless design ($\text{Re}[\sigma_Y] \rightarrow 0$) or across the zone with $\text{Im}[\sigma_X] \cong 3.5/\eta_0$, as also indicated in Fig. 6(a). In Fig. 7(b), we decrease the distance between the two monolayers ($L = 0.01\lambda$) and the highest Q performances are detected at the same regions as in Fig. 6(b) but are of much lower levels. Obviously, when both $\text{Im}[\sigma_X]$ and $\text{Re}[\sigma_Y]$ vanish, the monolayer is fully transparent and thus $Q = 1$ is not dependent on the implicit tilts of the axes (φ_1, φ_2). Note that the low-performance parametric locus is asymmetric with respect to $\text{Im}[\sigma_X] = 0$ and becomes clear that plasmonic designs ($\text{Im}[\sigma_X] < 0$) are more vulnerable to losses than the dielectric ones ($\text{Im}[\sigma_X] > 0$), for both Figs. 7(a) and 7(b).

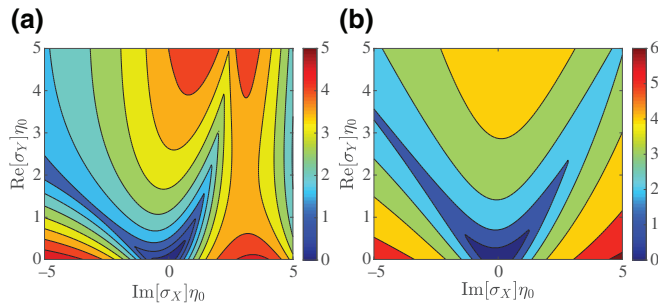


FIG. 7. Maximum signal enhancement $10 \log_{10} Q$ (in decibels) by regulating the optical twists (φ_1, φ_2) as a function of the imaginary part of normalized surface conductivity along one direction ($\text{Im}[\sigma_X]\eta_0$) and the real part of the respective quantity along the other direction ($\text{Re}[\sigma_Y]\eta_0$), for two different distances between the two monolayers: (a) $L = 0.05\lambda$ and (b) $L = 0.01\lambda$.

B. Signal spatial distribution

In order to understand the power enhancement into the cavity formed by the two anisotropic monolayers, it would be meaningful to show the variation of the electric field $|\mathbf{E}(z)|^2$ across the normal-to-interfaces z axis. In Fig. 8(a), we pick the optimal scenario from Fig. 6(a) corresponding to $L/\lambda = 0.05$ and represent the spatial distribution of the signal in two scenarios: (i) when $\varphi_2 = \varphi_1$ and (ii) when φ_2 equals to its magic value. It is noteworthy that the proposed rotation not only boosts the signal between the sheets but also reverts the trend from increasing to decreasing with respect to z . However, the field behind the bilayer ($z > L$) gets also significantly amplified while the reflections are mitigated since the overall signal for $z < 0$ approaches the incident unitary level.

In Fig. 8(b), we repeat the calculations of Fig. 8(a) after choosing the best design from Fig. 6(b) corresponding to $L/\lambda = 0.01$. In the one curve (red color), both tilts (φ_1, φ_2) are optimally selected, meaning that we have an electromagnetically analogous magic-angle effect, and with the other curve (blue color) we show the signal $|\mathbf{E}(z)|^2$ when both angles are equal to the optimal value of φ_1 . Once again, the increase in the power between the two monolayers is substantial and the design is almost transparent to the incoming illumination, admitting practically all the external field to penetrate into the cavity.

As implied above, the suppression of reflection is not a trivial result since the two monolayers are positioned very close to each other (small L/λ) and thus Fabry-Perot resonances are not possible. Suitable in-plane rotations of the impedance sheets render the bilayer practically transparent to the incoming illumination and, thus, the signal in between is almost equal to the incident magnitude; more substantial values are not possible since the two metasurfaces are free standing without denser substrates. One may remark that larger signal concentration across the

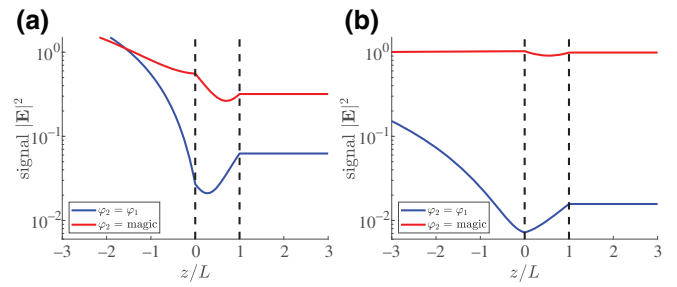


FIG. 8. Spatial distribution of the electric field signal $|\mathbf{E}|^2$ with respect to the longitudinal distance z/L when the two monolayers have the same optical axis twists ($\varphi_2 = \varphi_1$) and when there is a magic angle between them. Two different distances between the two monolayers are considered: (a) $L = 0.05\lambda$ (with $\sigma_X = 3.1i/\eta_0$ and $\sigma_Y = -10i/\eta_0$) and (b) $L = 0.01\lambda$ (with $\sigma_X = 10i/\eta_0$ and $\sigma_Y = -10i/\eta_0$).

cavity can be achieved if a point source [59] is positioned between the monolayers. However, our intention is to identify which configuration leads to significant field enhancement in the presence of mildly varying background waves instead of using hotspots to excite locally the system; to put it concisely, we are searching for optimal structures, not optimal feedings.

One of the major objectives of this work is to demonstrate a dramatic change in the behavior of the bilayer structure simply by rotating the optical axes. Such an operational switch has mainly to do with the field developed between the two monolayers, namely, with the power quantity P defined by Eq. (9) as well as with the metric Q that compares P with the case of zero relative tilt ($\varphi_2 - \varphi_1 = 0$). To understand that high scores of P (and, accordingly, Q) are quite challenging to hit, we show in Fig. 9(a) the electric field signal $|\mathbf{E}|^2$ (in decibels) across the cavity ($0 < z < L$) while sweeping all possible tilts ($\varphi_2 - \varphi_1$); with the blue dashed line, we denote the optimal level of relative rotation. It is clear that retaining substantial field between the flakes while being externally excited is not trivial since the configuration is free standing (vacuum background); as a result, $|\mathbf{E}|^2$ rarely surpasses the intensity of incoming wave. Note, additionally, that across the central angular sector $|\varphi_2 - \varphi_1| < 45^\circ$, the signal is very weak while the represented quantity is, on average, declining with z .

It is noteworthy that the pattern is almost symmetric with respect to $(\varphi_2 - \varphi_1)$ and, importantly, that maximal field concentration occurs for a very narrow range of $(\varphi_2 - \varphi_1)$ in the vicinity of the optimal tilt. In Fig. 9(b), we consider metasurfaces of elliptic type ($\text{Im}[\sigma_X], \text{Im}[\sigma_Y] > 0$), contrary to Fig. 9(a), where hyperbolic ($\text{Im}[\sigma_X]\text{Im}[\sigma_Y] < 0$) structures are employed. Once again, the sign of $(\varphi_2 - \varphi_1)$ is found to play little role but the magnitude of the recorded signal is much smaller compared to that of

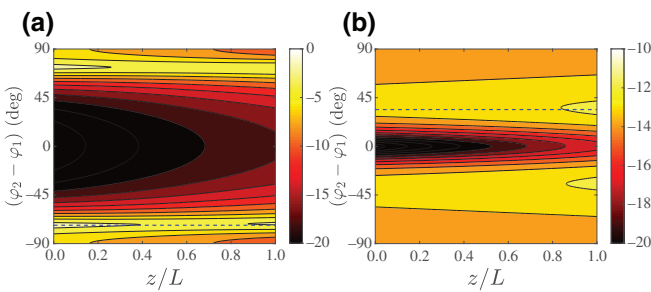


FIG. 9. The electric field signal $10 \log_{10} |\mathbf{E}|^2$ (in decibels) as a function of the longitudinal coordinate z/L and the relative rotation $(\varphi_2 - \varphi_1)$ of the monolayers for (a) hyperbolic metasurfaces ($\sigma_X = +9i/\eta_0$, $\sigma_Y = -8.5i/\eta_0$) and (b) elliptic metasurfaces ($\sigma_X = +9i/\eta_0$, $\sigma_Y = +0.5i/\eta_0$). Blue dashed lines indicate the optimal tilt levels. Distance between monolayers is $L/\lambda = 0.01$.

Fig. 9(a). Such a feature is attributed to the elliptic monolayers, which, unlike hyperbolic ones, are less successful in matching themselves with the vacuum background (for $L \ll \lambda$). Finally, one may remark the increasing trend of $|\mathbf{E}|^2$ with respect to z , contrary to the example of Fig. 9(a).

C. Interlayer spacing effect

In Fig. 10, we focus on the two monolayers optimized when kept at distance $L = 0.01\lambda$ and examine the behavior of the signal enhancement when the rotation angles of optical axes and the size of the cavity change. Indeed, there is no interest in investigating optimal setups at various interlayer spacings since maximal Q is a decreasing function of L/λ ; however, it is intriguing to observe the behavior of an optimized system at a given L/λ , once that distance varies.

In Fig. 10(a), we represent the metric Q across the map of optical length L/λ and the tilt of the first monolayer φ_1 . The operational point as derived from the optimization in Fig. 6(b) is denoted by a blue circle and the best φ_1 angle for $L = 0.01\lambda$ is marked by a red dashed line. One directly notices that for an increasing L/λ a substantial drop occurs in the recorded Q while for an intermediate zone of distances, two strong local maxima appear. These two “bright” parametric strips merge into one as the size of the bilayer shrinks, located around $\varphi_1 \cong 30^\circ$. Note that for $L > 0.05\lambda$ the metric increases again as dictated by the Fabry-Perot dynamics of the considered structure.

In Fig. 10(b), we represent the quantity Q on the plane $(L/\lambda, \varphi_2)$ this time. Again, two regions of significant field enhancement are formulated but one of them gives much stronger signal concentration than the other. Tuning the parameter φ_2 seems that it can lead to much higher Q at smaller distances compared to sweeping φ_1 . It can be attributed to the fact that the second flake interacts with a beam already filtered through the first monolayer and thus is easier to achieve high matching.

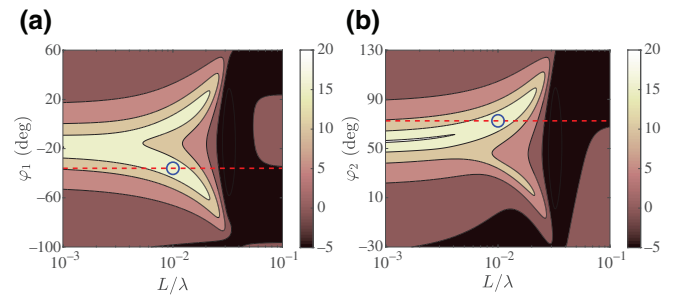


FIG. 10. The signal enhancement metric $10 \log_{10} Q$ (in decibels) as a function of the distance between the monolayers L/λ and (a) the optical twist of the first monolayer φ_1 , (b) the optical twist of the second monolayer φ_2 . The blue circles denote the optimal designs and the red dashed lines indicate the optimal levels of twists (φ_1, φ_2) for $L = 0.01\lambda$. Plot parameters are $\sigma_X = 10i/\eta_0$, $\sigma_Y = -10i/\eta_0$.

V. CONCLUSIONS

Two monolayers of a 2D anisotropic substance are placed close to each other and get normally illuminated. If one properly rotates their optical axes, the electromagnetic signals into the formed cavity become substantially enhanced and, as a consequence, state transitions are strongly encouraged. Our results constitute an electromagnetic version of the findings related to the magic-angle regimes in twisted bilayers of graphene and may inspire the next experimental and theoretical efforts towards versatile photonic design by simply rotating the employed impedance metasurfaces.

An interesting expansion of the present work would be to investigate multiple flakes of 2D materials and identify optimal setups into a multidimensional parametric space referring to the tilts of each sheet. In addition, the distances between each pair of consecutive components may vary to allow for ultrasharp resonances involving the energy distribution across the regarded layout. Biaxial or even fully anisotropic 2D media can be alternatively employed for performing effective twists of their optical axes by controlling the external biases to accomplish a number of electromagnetic operations within a few-atom-thick configuration.

ACKNOWLEDGMENTS

This work is partially supported by Nazarbayev University Faculty Development Competitive Research Grant No. 021220FD4051 (“Optimal design of photonic and quantum metamaterials”).

- [1] M. Tinkham, *Introduction to Superconductivity* (Dover Publications, Mineola, New York, NY, USA, 2004).
- [2] H. K. Onnes, Investigations into the properties of substances at low temperatures, which have led, amongst other things, to the preparation of liquid helium, Nobel Lecture, Stockholm, Sweden (1913).
- [3] J. Bardeen, L. N. Cooper, and J. R. Schrieffer, Theory of superconductivity, *Phys. Rev.* **108**, 1175 (1957).
- [4] I. Giaever, Energy Gap in Superconductors Measured by Electron Tunneling, *Phys. Rev. Lett.* **5**, 147 (1960).
- [5] A. J. Leggett, A theoretical description of the new phases of liquid He, *Rev. Mod. Phys.* **47**, 331 (1975).
- [6] J. G. Bednorz and K. A. Muller, Possible high- T superconductivity in the Ba-La-Cu-O system, *Z. Phys. B* **64**, 189 (1986).
- [7] G. R. Stewart, Superconductivity in iron compounds, *Rev. Mod. Phys.* **83**, 1589 (2011).
- [8] E. A. Ekimov, V. A. Sidorov, E. D. Bauer, N. N. Mel’nik, N. J. Curro, J. D. Thompson, and S. M. Stishov, Superconductivity in diamond, *Nature* **428**, 542 (2004).
- [9] K. L. Schepler, M. Yessenov, Y. Zhiyenbayev, and A. F. Abouraddy, Space-time surface plasmon polaritons: A new propagation-invariant surface wave packet, *ACS Photonics* **7**, 2966 (2020).
- [10] M. R. Norman, The challenge of unconventional superconductivity, *Science* **332**, 196 (2011).
- [11] Y. Cao, V. Fatemi, S. Fang, K. Watanabe, T. Taniguchi, E. Kaxiras, and P. Jarillo-Herrero, Unconventional superconductivity in magic-angle graphene superlattices, *Nature* **556**, 43 (2018).
- [12] Y. Cao, V. Fatemi, A. Demir, S. Fang, S. L. Tomarken, J. Y. Luo, J. D. Sanchez-Yamagishi, K. Watanabe, T. Taniguchi, E. Kaxiras, R. C. Ashoori, and P. Jarillo-Herrero, Correlated insulator behaviour at half-filling in magic-angle graphene superlattices, *Nature* **556**, 80 (2018).
- [13] F. Wu, A. H. MacDonald, and I. Martin, Theory of Phonon-Mediated Superconductivity in Twisted Bilayer Graphene, *Phys. Rev. Lett.* **121**, 257001 (2018).
- [14] Y. Xie, B. Lian, B. Jäck, X. Liu, C. Chiu, K. Watanabe, T. Taniguchi, B. A. Bernevig, and A. Yazdani, Spectroscopic signatures of many-body correlations in magic-angle twisted bilayer graphene, *Nature* **572**, 101 (2019).
- [15] G. Chen, A. L. Sharpe, P. Gallagher, I. T. Rosen, E. J. Fox, L. Jiang, B. Lyu, H. Li, K. Watanabe, T. Taniguchi, J. Jung, Z. Shi, D. Goldhaber-Gordon, Y. Zhang, and F. Wang, Signatures of tunable superconductivity in a trilayer graphene Moiré superlattice, *Nature* **572**, 215 (2019).
- [16] Y. Jiang, X. Lai, K. Watanabe, T. Taniguchi, K. Haule, J. Mao, and E. Y. Andrei, Charge order and broken rotational symmetry in magic-angle twisted bilayer graphene, *Nature* **573**, 91 (2019).
- [17] A. Kerelsky, L. J. McGilly, D. M. Kennes, L. Xian, M. Yankowitz, S. Chen, K. Watanabe, T. Taniguchi, J. Hone, C. Dean, A. Rubio, and A. N. Pasupathy, Maximized electron interactions at the magic angle in twisted bilayer graphene, *Nature* **572**, 95 (2019).
- [18] G. Tarnopolsky, A. J. Kruchkov, and A. Vishwanath, Origin of Magic Angles in Twisted Bilayer Graphene, *Phys. Rev. Lett.* **122**, 106405 (2019).
- [19] Z. Song, Z. Wang, W. Shi, G. Li, C. Fang, and B. A. Bernevig, All Magic Angles in Twisted Bilayer Graphene are Topological, *Phys. Rev. Lett.* **123**, 036401 (2019).
- [20] B. Lian, Z. Wang, and B. A. Bernevig, Twisted Bilayer Graphene: A Phonon-Driven Superconductor, *Phys. Rev. Lett.* **122**, 257002 (2019).
- [21] S. Carr, D. Massatt, S. Fang, P. Cazeaux, M. Luskin, and E. Kaxiras, Twistrionics: Manipulating the electronic properties of two-dimensional layered structures through their twist angle, *Phys. Rev. B* **95**, 075420 (2017).
- [22] E. Andrei and A. MacDonald, Graphene bilayers with a twist, *Nat. Mater.* **19**, 1265 (2020).
- [23] U. Zondiner, A. Rozen, D. Rodan-Legrain, Y. Cao, R. Queiroz, T. Taniguchi, K. Watanabe, Y. Oreg, F. Oppen, A. Stern, E. Berg, P. Jarillo-Herrero, and S. Ilani, Cascade of phase transitions and Dirac revivals in magic-angle graphene, *Nature* **582**, 203 (2020).
- [24] A. Uri, S. Grover, Y. Cao, J. Crosse, K. Bagani, D. Rodan-Legrain, Y. Myasoedov, K. Watanabe, T. Taniguchi, P. Moon, M. Koshino, P. Jarillo-Herrero, and E. Zeldov, Mapping the twist-angle disorder and Landau levels in magic-angle graphene, *Nature* **581**, 47 (2020).
- [25] X. Liu, Z. Hao, E. Khalaf, J. Lee, Y. Ronen, H. Yoo, D. Najafabadi, K. Watanabe, T. Taniguchi, A. Vishwanath, and

- P. Kim, Tunable spin-polarized correlated states in twisted double bilayer graphene, *Nature* **583**, 221 (2020).
- [26] P. Stepanov, I. Das, X. Lu, A. Fahimniya, K. Watanabe, T. Taniguchi, F. Koppens, J. Lischner, L. Levitov, and D. Efetov, Untying the insulating and superconducting orders in magic-angle graphene, *Nature* **583**, 375 (2020).
- [27] C. Shen, Y. Chu, Q. Wu, N. Li, S. Wang, Y. Zhao, J. Tang, L. Jieying, J. Tian, K. Watanabe, T. Taniguchi, R. Yang, Z. Meng, D. Shi, O. Yazyev, and G. Zhang, Correlated states in twisted double bilayer graphene, *Nat. Phys.* **16**, 520 (2020).
- [28] A. C. Tasolamprou, A. D. Kouloklidis, C. Daskalaki, C. P. Mavidis, G. Kenanakis, G. Deligeorgis, Z. Viskadourakis, P. Kuzhir, S. Tzortzakis, M. Kafesaki, E. N. Economou, and C. M. Soukoulis, Experimental demonstration of ultra-fast THz modulation in a graphene-based thin film absorber through negative photoinduced conductivity, *ACS Photonics* **3**, 720 (2019).
- [29] F. Vries, E. Portolés, G. Zheng, T. Taniguchi, K. Watanabe, T. Ihn, K. Ensslin, and P. Rickhaus, Gate-defined Josephson junctions in magic-angle twisted bilayer graphene, *Nat. Nanotechnol.* **16**, 760 (2021).
- [30] G. Hu, C. Zheng, J. Ni, C. Qiu, and A. Alù, Enhanced light-matter interactions at photonic magic-angle topological transitions, *Appl. Phys. Lett.* **118**, 211101 (2021).
- [31] M. Mattheakis, C. A. Valagianopoulos, and E. Kaxiras, Epsilon-near-zero behavior from plasmonic Dirac point: Theory and realization using two-dimensional materials, *Phys. Rev. B* **94**, 201404(R) (2016).
- [32] A. Sihvola, *Electromagnetic Mixing Formulae and Applications*, IEEE Electromagnetic Waves Series (Institution of Electrical Engineers, London, 1999).
- [33] D. L. Sounas and C. Caloz, Electromagnetic nonreciprocity and gyrotropy of graphene, *Appl. Phys. Lett.* **98**, 021911 (2011).
- [34] C. A. Valagianopoulos, M. Mattheakis, S. N. Shirodkar, and E. Kaxiras, Manipulating polarized light with a planar slab of black phosphorus, *J. Phys. Commun.* **1**, 045003 (2017).
- [35] J. S. Gomez-Diaz, M. Tymchenko, and A. Alù, Hyperbolic metasurfaces: Surface plasmons, light-matter interactions, and physical implementation using graphene strips, *Opt. Mater. Express* **5**, 246047 (2015).
- [36] O. V. Kotov and Yu. E. Lozovik, Enhanced optical activity in hyperbolic metasurfaces, *Phys. Rev. B* **96**, 235403 (2017).
- [37] C. A. Valagianopoulos, On measuring the permittivity tensor of an anisotropic material from the transmission coefficients, *Prog. Electromagn. Res. B* **9**, 105 (2008).
- [38] Y.-W. Son, M. L. Cohen, and S. G. Louie, Half-metallic graphene nanoribbons, *Nature* **444**, 347 (2006).
- [39] D. V. Kosynkin, A. L. Higginbotham, A. Sinitskii, J. R. Lomeda, A. Dimiev, B. K. Price, and J. M. Tour, Longitudinal unzipping of carbon nanotubes to form graphene nanoribbons, *Nature* **458**, 872 (2009).
- [40] H. Sakaguchi, S. Song, T. Kojima, and T. Nakae, Homochiral polymerization-driven selective growth of graphene nanoribbons, *Nat. Chem.* **9**, 57 (2017).
- [41] L. Zhang, X. Zeng, and X. Wang, Programmable hydrogenation of graphene for novel nanocages, *Sci. Rep.* **3**, 3162 (2013).
- [42] X. Wang, J. Ma, W. Zheng, S. Osella, N. Arisnabarreta, J. Droste, G. Serra, O. Ivashenko, A. Lucotti, D. Beljonne, *et al.*, Cove-edged graphene nanoribbons with incorporation of periodic zigzag-edge segments, *J. Am. Chem. Soc.* **144**, 228 (2022).
- [43] M. C. Watts, L. Picco, F. S. Russell-Pavier, P. L. Cullen, T. S. Miller, S. P. Bartuś, O. D. Payton, N. T. Skipper, V. Tileli, and C. A. Howard, Production of phosphorene nanoribbons, *Nature* **568**, 216 (2019).
- [44] Z. Liu, Y. Sun, H. Cao, D. Xie, W. Li, J. Wang, and A. K. Cheetham, Unzipping of black phosphorus to form zigzag-phosphorene nanobelts, *Nat. Commun.* **11**, 3917 (2020).
- [45] H. Zeng, C. Zhi, Z. Zhang, X. Wei, X. Wang, W. Guo, Y. Bando, and D. Golberg, “White graphenes”: Boron nitride nanoribbons via boron nitride nanotube unwrapping, *Nano Lett.* **10**, 5049 (2010).
- [46] T. Wu, Y. Luo, S. A. Maier, and L. Wei, Phase-matching and Peak Nonlinearity Enhanced Third-Harmonic Generation in Graphene Plasmonic Coupler, *Phys. Rev. Appl.* **11**, 014049 (2019).
- [47] V. Semenenko, S. Schuler, A. Centeno, A. Zurutuza, T. Mueller, and V. Perebeinos, Plasmon-plasmon interactions and radiative damping of graphene plasmons, *ACS Photonics* **5**, 3459 (2018).
- [48] S.-X. Xia, X. Zhai, L.-L. Wang, Q. Lin, and S.-C. Wen, Localized plasmonic field enhancement in shaped graphene nanoribbons, *Opt. Express* **24**, 16336 (2016).
- [49] M. H. Rezaei and A. Zarifkar, Dielectric-loaded graphene-based plasmonic multilogic gate using a multimode interference splitter, *Appl. Opt.* **57**, 10109 (2018).
- [50] C. Valagianopoulos, A. Sarsen, and A. Alù, Angular memory of photonic metasurfaces, *IEEE Trans. Antennas Propag.* **69**, 7720 (2021).
- [51] J.-W. Jiang, B.-S. Wang, and T. Rabczuk, Acoustic and breathing phonon modes in bilayer graphene with Moiré patterns, *Appl. Phys. Lett.* **101**, 023113 (2012).
- [52] M. Koshino and Y.-W. Son, Moiré phonons in twisted bilayer graphene, *Phys. Rev. B* **100**, 075416 (2019).
- [53] A. I. Cucemasov, D. L. Nika, and A. A. Balandin, Phonons in twisted bilayer graphene, *Phys. Rev. B* **88**, 035428 (2013).
- [54] K. Ueno, S. Nakamura, H. Shimotani, A. Ohtomo, N. Kimura, T. Nojima, H. Aoki, Y. Iwasa, and M. Kawasaki, Electric-field-induced superconductivity in an insulator, *Nat. Mater.* **7**, 855 (2008).
- [55] J. Shiogai, Y. Ito, T. Mitsuhashi, T. Nojima, and A. Tsukazaki, Electric-field-induced superconductivity in electrochemically etched ultrathin FeSe films on SrTiO₃ and MgO, *Nat. Phys.* **12**, 42 (2016).
- [56] M. Rasolt and Z. Tesanović, Theoretical aspects of superconductivity in very high magnetic fields, *Rev. Mod. Phys.* **64**, 709 (1992).
- [57] S. Uji, H. Shinagawa, T. Terashima, T. Yakabe, Y. Terai, M. Tokumoto, A. Kobayashi, H. Tanaka, and H. Kobayashi, Magnetic-field-induced superconductivity in a two-dimensional organic conductor, *Nature* **410**, 908 (2001).
- [58] A. N. Papadimopoulos, A. Duspayev, N. L. Tsitsas, N. V. Kantartzis, and C. Valagianopoulos, Wavefront engineering with optimally loaded absorbing metamirrors, *Phys. Rev. B* **103**, 165307 (2021).
- [59] S.-Y. Zhu, G.-B. Wu, S. W. Pang, and C. H. Chan, Compact terahertz dielectric folded metasurface, *Adv. Opt. Mater.* **10**, 2101663 (2022).